Chapter 8

Small Molecules and Peptides Inside Carbon Nanotubes: Impact of Nanoscale Confinement

Peng Xiu , Zhen Xia and Ruhong Zhou

Additional information is available at the end of the chapter

http://dx.doi.org/10.5772/51453

1. Introduction

Carbon-based nanoparticles and nanostructures, such as carbon nanotubes (CNTs), have drawn great attention in both academia and industry due to their wide potential applications. Owing to their well-defined one-dimensional (1D) interior, CNTs serve as desirable materials for encapsulating molecules, such as water [1-4], ionic liquid [5], drug molecules [6], and biomolecules [7]. The nanoscale confinement of CNTs have considerable impact on the inner molecules, including changes in their structure, size distribution, surface area, and dynamics, thus leading to many interesting and striking properties that are quite different from those in bulk [1-5, 7-9]. For example, nanoscale confinement of CNTs can give rise to ordered structure and extra-fast motion of water molecules [1-4], significantly enhanced activity of catalytic particles [8], phase transition of ionic liquids from liquid to high-melting-point crystal [5], and denatured structures of peptide helices [9]. In particular, recent studies [10-13] have shown that these CNT-based nanomaterials can be used as a new paradigm of diagnostic and therapeutic tools, which is beyond the traditional organic chemistry based therapeutics in the current pharmacology. Before their wide applications in the biomedical filed, the effects of CNTs on biomolecules (and drug molecules) need to be understood thoroughly [14-20].

In this book chapter, we review some of our recent works [21-24], with large scale molecular dynamics (MD) simulations using massively parallel supercomputers such as IBM Blue Gene, on the nanoscale confinement of both small molecules and peptides inside the CNT, which demonstrate wide implications in nanoscale signal processing, single-file transportation, drug delivery, and even cytotoxicity. The structure of this chapter will be organized as following. First, we show that water molecules confined within a Y-shaped CNT can realize the molecular signal conversion and multiplication, due to the surprisingly strong dipole-

induced orientation ordering of confined water wires [25]. Second, we find a striking phenomen that urea can induce the drying of CNTs and result in single-file urea wires. The unique properties of a urea wire as well as its biological and technological implications are discussed [22, 23]. Third, we show that nanoscale confinement can catalyze the chiral transition of chiral molecules. We further explore the molecular mechanism of CNT-catalyzed enantiomerization and provide some implications for drug delivery [24]. Last, we investigate the effect of confinement of CNT on three important secondary structural motifs of proteins – a hairpin turn, a helix, and a beta-sheet.

2. Results

2.1. Water-mediated signal multiplication with Y-shaped nanotubes

Uunderstanding the molecular-scale signal transmission (amplification, shunting, etc) has attracted intensive attentions in recent years because it is of particular importance in many physical, chemical, and biological applications, such as molecular switches, nano-gates, and biosensors [26-29]. However, due to the intrinsic complexity of these nano-systems and the significant noises coming from thermal fluctuations as well as interferences between branch signals, the molecular details are far from well understood. On the other hand, water molecules confined within nanochannels exhibit structures and dynamics quite different from bulk [3], which might provide a medium for molecular signal transmission. Water molecules inside CNT with a suitable diameter can form a single-file hydrogen-bonded molecular wire, with the concerted water dipole orientations, i.e., either parallel or antiparallel to the CNT axis [1, 30, 31]. The characteristic time for reorientation of the dipole orientation of water wire is in the range of 2–3 ns for CNT with a length of 1.34 nm [1], and the water wire inside a nanochannel can remain dipole-orientation-ordered up to macroscopic lengths of ~ 0.1 mm, with durations up to ~ 0.1 s [30]. If we can "tune" the orientation of a water molecule at one end, we might be able to control the orientations of all water molecules in the molecular wire and even amplify and shunt the orientation signal.

Recently, Y-shaped nanotubes have been successfully fabricated by means of many different methods [32-34]. These nanotubes have been found to exhibit both electrical switching and logic behaviour [27, 35]. In the following, we will show that single-file water wires confined within a Y-shaped single-walled CNT (hereafter referred to it as Y-SWNT, see Fig. 1) can perform both signal amplification and shunting, ignited by a single electron, because of the surprisingly strong interactions between water molecules at the Y-junction. We construct Y-SWNT by jointing three (6, 6) uncapped armchair single-wall CNTs (SWNTs) together symmetrically along three directions neighbouring 120° one another. An external charge, q, is positioned at the centre of a second carbon ring of the main nanotube (see Fig. 1) to monitor the dipole orientation of water wire inside the tube. All carbon atoms were fixed and an opposite charge was assigned at the edge of simulated boxes to keep the whole system charge-neutral. MD simulations were carried out in NVT ensemble (300K, 1atm) with Gromacs 3.3.3 [36]. The TIP3P [37] water model was used.

http://dx.doi.org/10.5772/51453

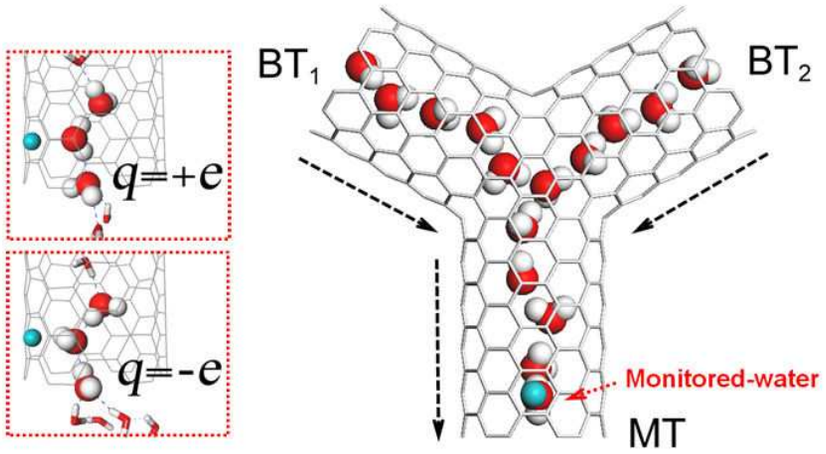

Figure 1. Schematic snapshot of the simulation system in side-view. The Y-SWNT consists of a main tube (MT) and two branch tubes (BT_1, BT_2) positioned in the same plane. Water molecules outside the nanotubes are omitted. The light blue sphere represents the imposed charge. The water molecule facing the external charge is referred to as "Monitored-water". The lengths of MT, BT_1 and BT_2 are 1.44 nm, 1.21 nm, and 1.21 nm, respectively. Insets: Enlarged part for the typical configurations: upper for q = -e and lower for q = +e. This figure is reproduced from ref. [21] with permission.

The simulations show that water molecules in the Y-SWNT form single-file hydrogen-bonded molecular wires. Although the water wires in different tubes interact at the Y-junction, all water's orientations are either parallel or anti-parallel to the nanotube axis, similar as the case of water wire in conventional SWNT [1]. To describe quantitatively the confined water's dipole orientation, we choose an angle ϕ_i between the dipole orientation of ith water molecule and the SWNT axis, and the average angle $\bar{\varphi}(t)$, which the average over all the water molecules inside a nanotube at some time t. The outward direction of the main tube and inward directions of the branch tubes are set as positive directions. The results are displayed in Fig. 2(A). It is clear that $\bar{\varphi}$ dominantly falls in two ranges for each nanotube, $10^\circ < \bar{\varphi} < 70^\circ$ and $110^\circ < \bar{\varphi} < 170^\circ$, indicating that the water molecules within each nanotube are nearly aligned. Furthermore, we have noticed that $\bar{\varphi}(t)$ for all tubes falls in the range from 10° to 70° when q = -e, with few fluctuations to larger values. In contrast, when q = +e, $\bar{\varphi}(t)$ for the main tube primarily falls into the range from 110° to 170°. For the branch tubes, $\bar{\varphi}(t)$ jumps between the two ranges. From the water orientations in each branch tube, we can easily identify the sign of the imposed charge, i.e., the charge signal at the main tube correctly transmits and is amplified/shunted to the two branch tubes.

To further characterize the molecular signal transmission, we define an integer $s(t)$: $s(t)$ = +1 when $10^\circ < \bar{\varphi} < 70^\circ$, and $s(t)$ = -1 when $110^\circ < \bar{\varphi} < 170^\circ$. We calculate the $P(t)$, defined as the occurrence probability of $s(t)$ = +1 from the start of the simulation until the time t in each tube. For a sufficiently long time, $P(t)$ in both branch tubes will approach 1.0 when q=-e, and approach 0.5 when q =+e since $\bar{\varphi}(t)$ falls in the two different ranges with an equal probability. Here, we set P_C = 0.8 as the threshold value to determine the charge. It is expected that $P > P_C$ indicates q = -e, and that $P < P_C$ indicates q = +e. From Fig. 2(B) we can see that, for both branch tubes, when q = -e, $P > P_C$ for t> 1 ns; when q = +e, $P < P_C$ for t> 8 ns. Consequently, the

charge signal at the main tube can be readily distinguished from the value of $P(t)$ in each branch tube within a time interval of ~8 ns.

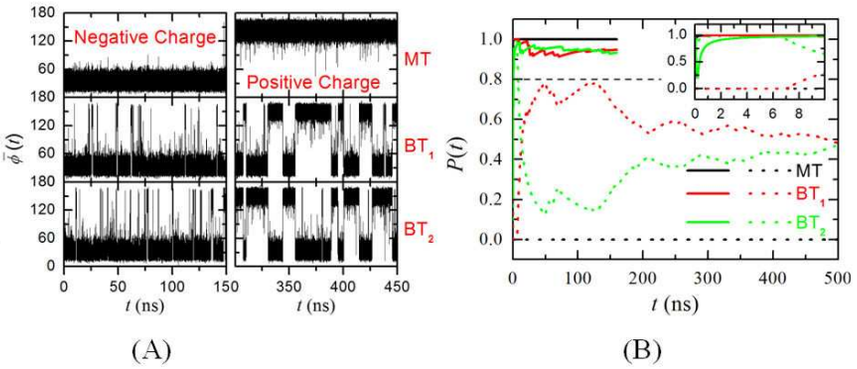

Figure 2. Trajectory of average dipole angle $\bar{\varphi}(t)$ of the water orientation and the probability of dipole orientation $P(t)$ in each tube in a Y-SWNT. (A) Average dipole angle in the main tube (MT), first branch tube (BT_1) and second branch tube (BT_2) for a negative charge (left) and a positive charge (right) in the main tube. (B) $P(t)$ in different tubes for a negative charge (solid lines) and a positive charge (dashed lines). $P(t)$ for a negative charge converges to about 1.0 within a few nanoseconds. This figure is reproduced from ref. [21] with permission.

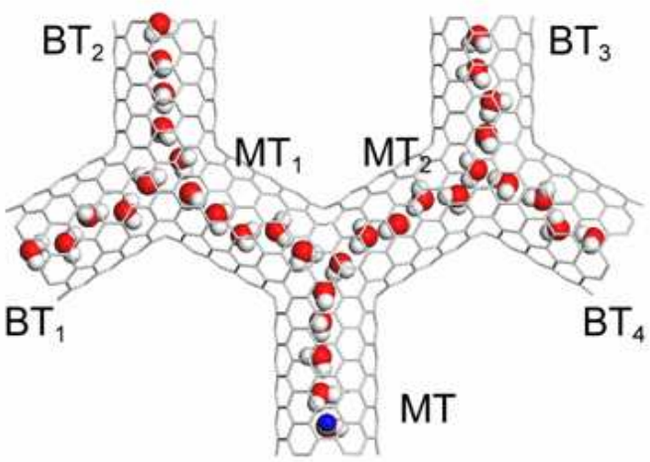

Figure 3. Snapshot of a three Y-junction (3Y-SWNT) system (side view). Colours match those in Fig. 1. The angle between any two neighbouring tubes at each Y-junction is 120˚. The lengths of the main tube (MT), two middle tubes denoted by MT_1 and MT_2, and four branch tubes denoted by BT_1, BT_2, BT_3 and BT_4 are 1.44 nm, 1.44 nm, and 1.21 nm, respectively. This figure is reproduced from ref. [21] with permission.

Careful examinations reveal that the external charge "monitors" the water molecule facing this charge (referred to as the "Monitored-water"); the Monitored-water determines the water orientations in the main tube; the uppermost water molecule in the main tube governs the dipole orientations of the bottommost water molecules in branch tubes and hence the water dipole orientations within both branch tubes (see ref. [21] for more discussions). In addition, we find that the response to the switching of the charge signal is very rapid, from a few nanoseconds to a few hundred nanoseconds: In response to $-e \rightarrow +e$ signal switching, the

time delay for the branch tubes is 40 ns on average with a maximal duration of 150 ns; in response to +*e*→-*e* polarity flip, it is only around 4ns.

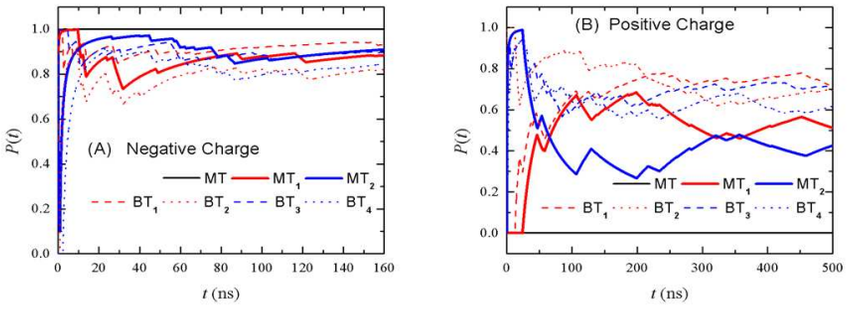

Figure 4. Probability *P*(*t*) in the main tube (black line), two middle tubes (blue and red solid lines), and four branch tubes (dashed lines) in response to a negative (A) and a positive (B) imposed charge signal. This figure is reproduced from ref. [21] with permission.

The charge signal can also be transmitted and amplified/shunted through additional channels. We have simulated a system with three Y-junctions where each of the outlet branch tubes forms a Y-junction connecting two more tubes (see Fig. 3). We refer the two middle tubes as MT_1 and MT_2, and the four branch tubes as BT_1, BT_2, BT_3 and BT_4. Fig. 4 shows the *P*(*t*) for different branch tubes. It is found that when t > 200 ns, $P(t) > P_C$ when q = -e, and $P(t) < P_C$ when q = +e, for all branch tubes. As a consequence, the charge signal at the main tube transmits to four branch tubes with a temporal resolution time of ~200 ns.

To summarize, by using MD simulations we show that a signal at the single-electron level can be converted and multiplied into two or more signals by water wires confined within a narrow Y-shaped CNT. This remarkable capability of signal transduction by Y-SWNT derives from the surprisingly strong dipole-induced ordering of such water wires, so that the concerted water orientations in the two branches of the Y-SWNT can be modulated by the orientation of water wire in the main channel. The response to the switching of the charge signal is found to be very rapid, from a few nanoseconds to a few hundred nanoseconds. To our knowledge, this is the first observation of the remarkable signal amplification and shunting with a Y-shaped nanotube at the atomic level and this observation may have significance for future applications in molecular-scale electronic devices. In addition, it is noteworthy that there are Y-shaped biological channels [38, 39], therefore, our findings might also provide useful insight into the molecular signal transmission in biological systems.

2.2. Molecular wire of urea and induced drying in carbon nanotubes

2.2.1. Molecular wire of urea inside narrow carbon nanotube

Molecules confined inside nanoscale space such as narrow nanotubes or membrane proteins can form one-dimensional (1D) molecular wires, which have attracted intense interest recently because of their scientific importance and potential applications in nanotechnology [1, 21, 40-56]. Among them, it is of particular interest in determining the structure and dynami-

cal behavior of water wires [1, 21, 40-49] which have been found to exist in narrow nanotubes[1, 21, 40-42, 46-48] and biological channels [43-45]. Water wires have many interesting properties, such as wavelike density distributions [1, 46], rapid and concerted motions [1, 40, 43], orientation-ordered structures and collective flips [1, 21, 41, 48], and excellent on-off gating behaviors [46, 47]. In addition, it has been observed that the methane [56], methanol [54], and gas molecules (O_2, H_2, and CO_2) [55] preferentially bind to the interiors of narrow SWNT over water and form 1D molecular wires. Despite the above progress, the properties of molecular wires have not been fully understood, particularly for the molecular wires formed by larger polar organic molecules.

Urea plays an important role in the metabolism of nitrogen-containing compounds by animals [57, 58], and serves as a common protein chemical denaturant and an important raw material in chemical industry. It is important to note that the biological urea channel dvUT (a urea transporter from the bacterium *Desulfovibrio vulgaris*) has a long (~ 16 Å) and narrow selectivity filter; this filter consists of closely spaced hydrophobic residues which allows dehydrated urea to permeate in single-file [58]. The hydrophobic SWNTs with appropriate diameters might serve as useful model systems for studying biological urea channel. The current simulations were based on TIP3P water model [37] and two commonly used urea models, namely, KBFF [59] and OPLS [60, 61] models. Below we mainly present the results for the KBFF case; the results for OPLS case are similar, and some of them are also shown as comparison. The simulation were performed using Gromacs 4.0.7 [62] in an NPT (300K, 1 atm) ensemble.

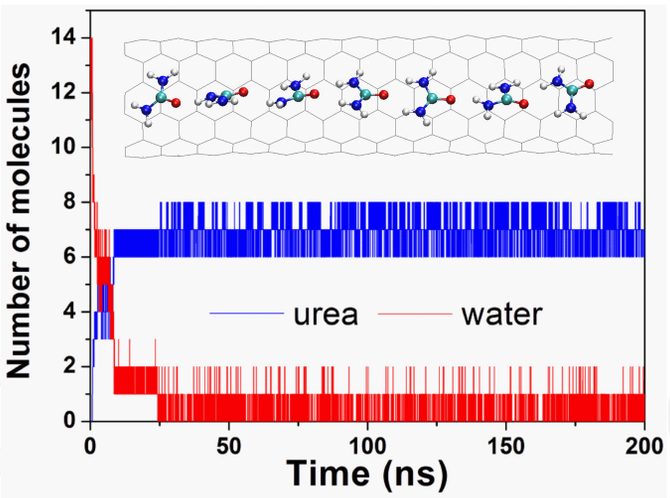

Figure 5. Number of urea (in blue; KBFF urea model is used) and water (in red) molecules within the 336-carbon (6, 6) SWNT as a function of simulation time, at 1 M urea concentration. Inset: Snapshot of a "perfect" urea wire.

We have performed MD simulation of 336-carbon (6, 6) SWNT (3.32 nm in length), solvated in aqueous urea with various urea concentrations (8M, 1 M and 0.5 M, with the simulation lengths 100 ns, 200 ns, and 200 ns, respectively). Fig. 5 shows the number of solvent (water/urea) molecules inside the SWNT in case of 1 M urea concentration during the course of simulation. Almost all water molecules inside the SWNT are replaced by urea within the first 25 ns. The confined urea molecules form a 1D "perfect" urea wire with a contiguous hydrogen-bond-

ed network in most of the simulation time, or occasionally forms a "defective" urea wire [with a very small number of "water defect(s)", commonly near the SWNT edge].

Table 1 summarizes the average number of urea ($\overline{N}_{urea}$) and water molecules ($\overline{N}_{water}$) inside the SWNT after the systems have reached equilibrium with various urea concentrations. Regardless of urea concentration and urea model used, finally, the SWNTs are nearly completely filled with urea molecules. Table 1 also shows the occurrence probability for "perfect" urea wire, P_{perfect}, which is high for most cases. These results indicate that urea has a robust capability to form uninterrupted molecular wire.

C_{urea}	KBFF			OPLS		
	$\overline{N}_{urea}$	$\overline{N}_{water}$	P_{perfect}	$\overline{N}_{urea}$	$\overline{N}_{water}$	P_{perfect}
0.5 M	7.03	0.29	72.6%	6.23	1.67	11.8%
1 M	7.09	0.16	84.0%	6.68	0.85	42.9%
8 M	7.10	0.03	96.7%	7.00	0.14	86.8%

Table 1. Average number of urea and water molecules ($f_{\text{drying}} = R_{\text{SWNT}} / R_{\text{bulk}}$ and $\bar{N}_{urea}$, respectively) inside the 336-carbon (6, 6) SWNT in equilibrium, together with occurrence probabilities for "perfect wire" (P_{perfect} [a]), with various urea concentrations (C_{urea}) and with different urea models.

Next, we explore the structure of the confined urea wire. We use the case of the 336-carbon (6, 6) SWNT in 8 M KBFF urea for illustration because P_{perfect} in this case is very high (see Table 1). We performed two independent 100 ns simulations under same conditions, denoted by case 1 and case 2, respectively. As shown in the inset of Fig. 5, urea molecules inside (6, 6) SWNT form a single-file structure with a contiguous hydrogen-bonded network and concerted dipole orientations [urea's dipole orientation approximates the dipole orientation of its carbonyl (-CO-) group]. Quantitatively, we have computed ϕ (the angle between a urea dipole and the nanotube axis). ϕ is found to fall in two ranges: the angle around 20º (case 1) and around 160º (case 2). No event of flipping between these two ranges is observed during the time period of 100 ns. Even for urea wire in 144-carbon (6, 6) SWNT, no flipping event is observed for KBFF urea, and 1~2 flipping events is observed for OPLS urea, during several independent 100 ns simulations. In contrast, the flipping of water wire inside 144-carbon (6, 6) SWNT occurs every 2~3 ns on average [1, 48]. Further analysis reveal that the lower flipping frequency of urea wire compared with water mainly comes from the larger physical dimension and higher polarity of urea [23].

The above findings have technological implications. Our previous reports [21, 25] have demonstrated water wires can mediate the signal conversion and multiplication because of their ordered 1D structure and collective flipping behavior. However, the very small size of the water and fast flipping of water wire make the experimental realization very difficult [25]. Urea wire has similar ordered 1D structure and flipping behavior as water wire but has a lower flipping frequency and a high molecular polarity which can facilitate the signal detection in practice (urea wire has longer response time [21] to switch its dipole orientation un-

der the influence of a change in charge signal). We therefore expect that urea wire can serve as a better candidate for signal transduction and multiplication.

Next, we have calculated the position distribution of urea along the nanotube axis. There are seven distinct, sharp peaks (with an average peak-to-peak value of ~ 4.6 Å), indicating that the urea wires are translationally ordered along the SWNT axis. The position distribution is found to be much sharper than water wire owing to the larger molecular size of urea (see ref. [23] for details).

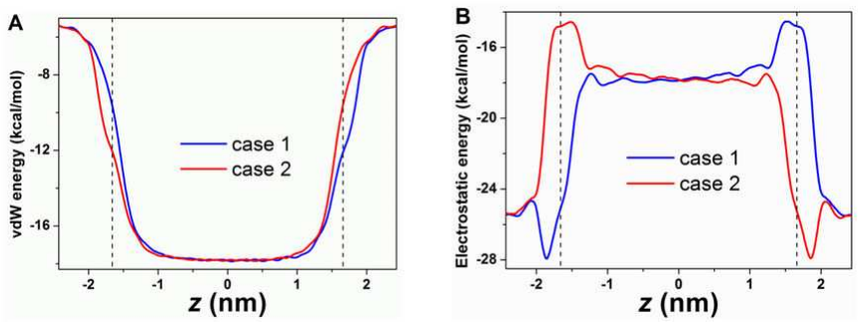

Figure 6. Potential energy profiles of urea along the axis of 336-carbon (6, 6) SWNT (8 M urea, KBFF urea model is used). (A) and (B) show the van der Waals (vdW) and electrostatic potentials, respectively. Case 1 and case 2 denote independent simulation under same conditions. The positions of SWNT inlet/outlet are indicated with dashed lines.

We have also calculated the interaction energies with the rest of the system for a urea molecule with respect to its axial distance from the geometrical center of SWNT (see Fig. 6). Interestingly, the vdW potential curves are approximately symmetric; whereas electrostatic potential curves are observably asymmetric, i.e., correlate to the inner urea's dipole orientations. Urea's asymmetric molecular partial charge distribution together with the extremely confined space result in the orientationally ordered structure (concerted dipole orientations) of molecular wire, thus breaking the symmetry of the system within a finite time period (more than 100 ns for the present case) and causing an asymmetric electrostatic potential.

Although single-file transport of water through SWNT has been intensively investigated in recent years [1, 40, 46-48], much less is known about the single-file transportation for organic small molecules. Here we explore the transport properties of urea wire and make a comparison with water wire. We have calculated the urea flow, defined as the total number of urea molecules per nanosecond that have entered from one end and leave the SWNT from the opposite side. Given that the biological urea channel dvUT [52] has a length of ~ 16 Å (the number of urea molecules accommodated in the selectivity filter is about 3), we chose the 144-carbon (6, 6) SWNT (13.5 Å in length) as the nanochannel, wherein the resulting urea wire also consists of ~ 3 urea molecules. To facilitate a direct comparison with water wire, we performed additional simulations for the SWNT immersed in pure water. The calculated average flows (averaged over three independent 100 ns simulations) are 0.73 ns^{-1} and 0.79 ns^{-1}, for KBFF and OPLS urea, respectively, and it is 16.2 ns^{-1} for water. Transportation of urea seems to be 20+ times slower than water. Fig. 7(A) displays the time evolution of urea flow from a typical simulation trajectory. The urea flow is low, with a maximal value of only 4 ns^{-1}; it vanishes fre-

quently, and the duration time of zero value can be up to 6 ns (e.g., t = 11 ns ~ 17 ns). In contrast, for water wire, its minimal flow is up to 7 ns^{-1}, and its maximal flow reaches a value of 32 ns^{-1}. Furthermore, we have studied the influence of urea concentrations (1 M ≤ C_{urea} ≤ 10 M) of the surrounding bath on urea's permeability through SWNT and find a maximal urea flow (~0.87 ns^{-1}) around a concentration of 5 M (see ref. [23] for more details).

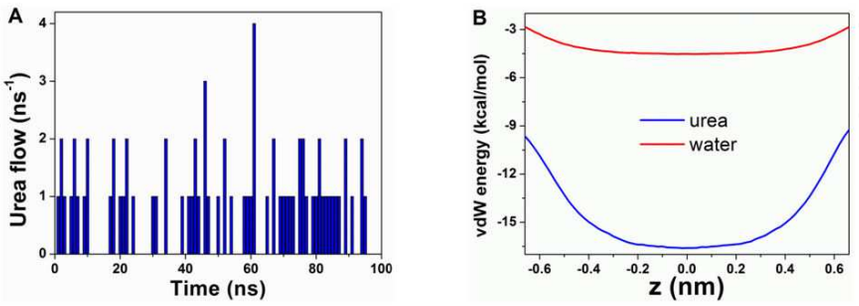

Figure 7. Single-file transport of urea through 144-carbon (6, 6) SWNT (8 M urea, using KBFF urea for demonstration) and the underlying physics. (A) Urea flow versus time from a typical trajectory. (B) The potential energy profiles along the SWNT axis for the urea wire (blue) and the water wire (red), respectively. The data for water derives from the control runs of SWNT immersed in pure water.

To understand the physical mechanism behind the enormously lower permeability of urea relative to water for SWNT, we have calculated the interaction energies of a inner urea/water molecule with the SWNT (the data for water derives from the control runs of SWNT immersed in pure water). Because the carbon atoms of SWNT are modeled as uncharged Lennard-Jones particles, there are only vdW interactions between urea/water and SWNT. As displayed in Fig 7(B), the potential valley for urea is much deeper than that for water, because urea has a stronger dispersion interaction with SWNT than water, which in turn leads to a much lower permeability of urea than water.

In this section, we have investigated the structure and dynamical behavior of urea wire inside the narrow SWNT. Even at relatively low urea concentration (e.g., 0.5 M), we have observed spontaneous and continuous filling of SWNT with a 1D urea wire. The resulting urea wire is translationally and orientationally ordered, with a contiguous hydrogen-bonded network and concerted dipole orientations of urea molecules. Despite the symmetric nature of SWNT, the urea's potential energy profile along SWNT is asymmetric, coming from asymmetric molecular partial charge distribution (or dipole moment) and the ordering of urea's dipole orientation under extremely confinement. Furthermore, we have studied the single-file transportation of confined urea, and find that urea flow decreases significantly (by a factor of ~ 20) compared to that of water, due to the fact that urea has a stronger dispersion interaction with SWNT than water. We also find a maximum in urea permeation around a concentration of 5 M. The studies on the urea wire confined inside SWNT not only help our understanding of the unique properties of confined polar organic molecules, but also present biological (biological urea channel) and technological (e.g., electronic devices for signal transduction and multiplication at nanoscale) implications.

2.2.2. Urea-induced drying of carbon nanotubes

In the previous section, we have demonstrated that urea can expel water inside a narrow SWNT [(6, 6) SWNT]. One may wonder if this phenomenon can persist in wider SWNT. To answer this, we performed MD simulations of (17, 8) SWNT (1.73 nm in diameter, it can accommodate several layers of urea and water) immersed in 8 M urea solution. Considering that there are some urea models commonly used in literature whose charge distributions are quite different [22], herein we have used five different urea models to test if the drying phenomenon is sensitive to force fields used.

The five urea models used in the current study are the OPLS [60, 61], KBFF [59], CHARMM (parameters derived from the CHARMM22 force field [63]), AMBER* [64], and AMBER [parameters derived from the file embedded in the AMBER 10 simulation package (University of California at San Francisco)] urea models. The simulation were performed using Gromacs 4.0.7 [62] in an NPT (300K, 1 atm) ensemble with the simulation lengths of 100 ns for all systems. In all cases, we observe that most of water molecules initially inside the SWNT (C_{urea} inside the SWNT is approximately 8 M from the initial solvation setup) are repelled from the SWNT within the first 10 ns; after that, the hydrophobic nanopores are dominantly occupied by urea. Table 2 lists the average number of urea and water molecules inside (17, 8) SWNT with different urea models. To quantitatively characterize the drying effect, we have calculated the "drying factor", f_{drying}, defined as following:

$$f_{\text{drying}} = R_{\text{SWNT}} / R_{\text{bulk}} \tag{1}$$

where R_{SWNT} and R_{bulk} are the ratios of the average number of urea to water molecules inside SWNT and in the bulk region, respectively. A larger f_{drying} means a stronger urea-induced drying effect. f_{drying} for different urea models are also shown in Table 2. In all cases, f_{drying} is very high, indicating that strong drying phenomena occur in all cases.

Model	$\overline{N}_{urea}$	$\overline{N}_{water}$	f_{drying}
OPLS	43.6	12.8	14.8
KBFF	37.9	25.7	6.40
CHARMM	45.5	6.6	29.9
AMBER*	49.6	5.9	36.8
AMBER	47.8	2.9	71.7

Table 2. Average number of urea ($\bar{N}_{urea}$) and water molecules ($\bar{N}_{water}$) inside (17, 8) SWNT together with the drying factors, f_{drying} (see text for the definition) with different urea models. These data were averaged over the time region wherein the systems have reached equilibrium (t ≥ 90 ns).

To understand the observed phenomenon of urea-induced drying of SWNTs, we have calculated the difference in average interaction energies for a solvent (urea/water) in bulk and in (17, 8) SWNT with the rest of the system. As the solvent molecules move from bulk into the (17, 8) SWNT, both urea and water lose electrostatic interaction energies, but urea gains more vdW energy than water (about 3~4 times larger than water), which mainly comes from the stronger dispersion interaction of urea than water with nanotube. As a consequence, after a solvent penetrates the SWNT, on average each urea gains 2.55~4.58 kcal/mol whereas each water loses 0.12~1.64 kcal/mol. It is noteworthy that the replacement of structurally confined water by larger urea (on average each urea molecule can replace ~2.5 water molecules) is also favorable in overall free energy due to an overall solvent entropy gain. In addition, the free energy analysis [by calculating the potential of mean force (PMF)] also support that the phenomenon of urea-induced drying of SWNT derives from the stronger dispersion interaction of urea with SWNT than water (see ref. [22] for details).

In conclusion, by using MD simulation we have observed a striking phenomenon of urea-induced drying of hydrophobic nanotubes and demonstrated the robustness of this phenomenon by using five different urea models. By decomposing the interaction energies for a solvent molecule into electrostatic and vdW components, we find that the drying phenomenon results from the stronger dispersion interaction of urea than water with nanotube. These results also have implications on understanding the urea-induced denaturation of proteins by providing further evidence of the potential existence of a "dry globule"-like transient state [65] during early stage of protein unfolding and the "direct interaction mechanism" whereby urea attacks protein directly via favorable dispersion interaction, rather than disrupts water structure as a "water breaker". In addition, this study points out the crucial role of dispersion interaction in the selective absorption of molecules inside hydrophobic nanopores [54-56], which might be important for nanoscience and nanotechnology.

2.3. Chirality switch of drug-like molecules inside boron-nitride nanotubes

Many basic building materials of organism, such as amino acids and saccharides, are chiral in nature. Understanding the molecular chirality is very important for pharmaceutical products because the biological systems have stereoselectivity [66]. Some molecules chiral stable in bulk systems may undergo conformational transitions in human body [67]. For example, in late 1950s and early 1960s, thalidomide caused serious damages to the fetal growth, known as the "thalidomide tragedy" [67, 68], which correlates to a chiral transition of thalidomide occurred in human body. Hence, good conformational stability is an important requirement for chiral molecules used in pharmaceutical products and drug delivery.

It is well-known that there are various nanoscale confinement environments in human body, but the effect of nano-confinement on molecular chirality is still poorly understood so far. Here we use MD simulations (employing Gromacs 3.3.1 [36]) to study the chiral transition of difluorobenzo[c]phenanthrene molecules ($C_{18}H_{12}F_2$, referred to as "D molecule") in single-walled boron-nitride nanotubes (SWBNNTs). Molecular systems can be chiral by asymmetrically arranging atoms in space around a center, axis, or plane, which are called point, axial, and planar chirality, respectively [69]. It has been reported using infrared laser

pulses that D molecule show the planar chirality transition between *P*-enantiomer and *M*-enantiomer, and the energy barrier for this transition in bulk was estimated to be only 6.7-8.0 kcal/mol [70]. The chiral character of enantiomers can be characterized by dihedral angle of four atoms (a-b-c-d) shown in Fig. 8(a). When the dihedral angle is averaged over a certain time period (0.1 ns is used), the value of the chiral character is positive for *P*-enantiomer and negative for *M*-enantiomer.

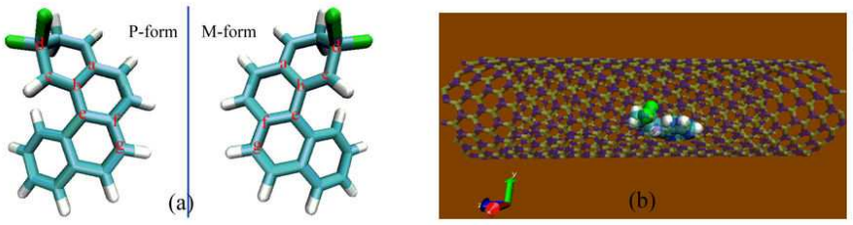

Figure 8. a) *P*- and *M*-form enantiomers of D molecule. The dihedral angle of four atoms (a-b-c-d) is used to identify the chiral geometry of different enantiomers. The e, f and g atoms are used to determine a plane of the D molecule. (b) Snapshot of D molecule inside a (15, 6) SWBNNT to illustrate the simulation system. This figure is reproduced from ref. [24] with permission.

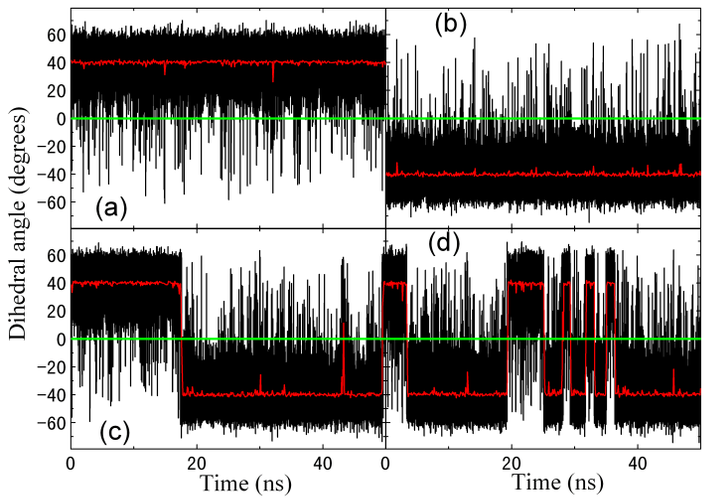

Figure 9. Time evolution of dihedral angle of the D molecule in a (15, 6) SWBNNT at different temperatures. (a) *P*-form at 420 K. (b) *M*-form at 420 K. (c) *P*-form at 440 K, showing chiral transition. (d) *P*-form at 460 K, showing chiral transition. This figure is reproduced from ref. [24] with permission.

Figs. 9(a) and (b) show the chiral character of *P*- and *M*-enantiomers inside a (15, 6) SWBNNT at 420 K. In all of 50 ns simulation times, the averaged values of dihedral angle keep their original signs, indicating that both *P*- and *M*-enantiomers are chiral stable at (and below) 420 K. When the temperature increases to 440 K, the chiral transitions occur, as

shown in Figs. 9(c) and (d). Similar phenomena have been observed in other SWBNNTs systems in which the transition occurs at different temperature thresholds.

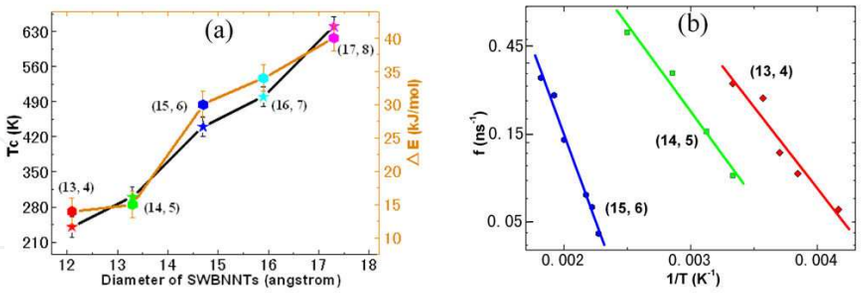

Figure 10. a) Transition critical temperature T_C (star representation, left axis) and corresponding interaction energy barrier ΔE between SWBNNT and D molecules in the chiral transition process (● representation, right axis). Symbols of the same color denote the data for the same SWBNNT. (b) The dependence of chiral transition frequency f on temperature T. Solid lines are fitted with the exponential functions $f = f_0 \exp(-E_a/k_B T)$ for different SWBNNTs. This figure is reproduced from ref. [24] with permission.

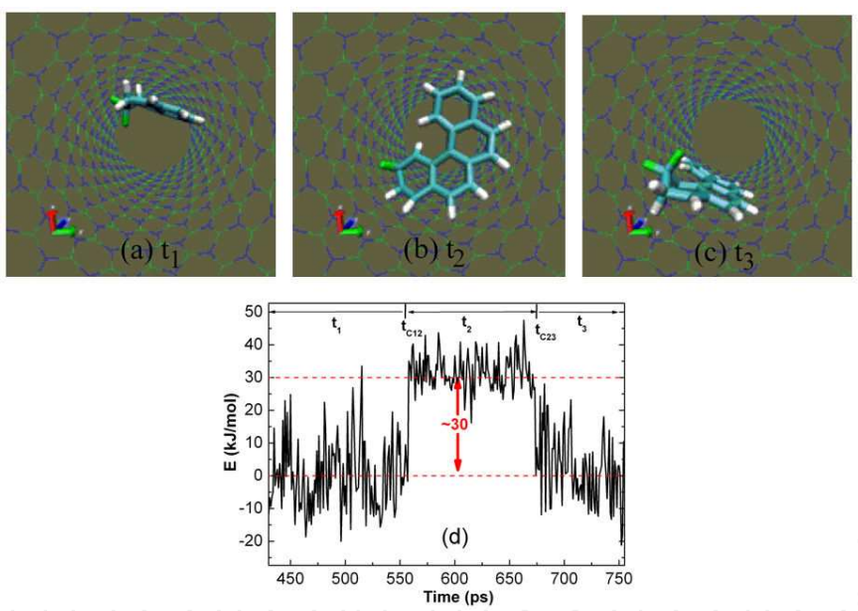

Figure 11. Typical configurations of D molecule and the corresponding interaction energies E inside (15, 6) SWBNNT in different time periods. t_1 and t_3 denote the time periods wherein the enantiomers are stable; t_2 denotes the time periods wherein the chiral transition occurs. This figure is reproduced from ref. [24] with permission.

We have computed the critical temperature T_C for chiral transitions for different SWBNNTs. Here T_C is defined as the temperature at which the enantiomers can transform within 30 ns, and meanwhile, the enantiomer keeps intact at T_C -20 K for 30 ns, for a large number of trajectories starting from different initial configurations, with the error bars of T_C approximately 20 K by this definition. As displayed in Fig. 10(a), T_C increases monotonically with the diameter of SWBNNT. We have also calculated the frequencies of chiral transition, f, for dif-

ferent temperatures inside various SWBNNTs, as shown in Fig. 10(b). The data can be fitted with the Arrhenius activation energy function ($f = f_0 \exp(-E_a/k_B T)$) very well, where E_a is the activation energy, k_B is the Boltzmann constant. For the current cases, f_0 = 937, 139, 276 ns^{-1}, and E_a = 36, 18, 17 kJ/mol, for (15, 6), (14, 5), and (13, 4) SWBNNTs, respectively.

Now we focus on how enantiomerization occurs in nanotubes and the mechanism behind those observations. The D molecule consists of four six-membered rings, with a nearly planar structure. At low temperatures, the D molecule prefers to cling to the inner surface of SWBNNT [with its rings parallel to the SWBNNT axis, see Fig. 11(a)]. It is observed that when chiral transition occurs, the D molecule changes its orientation first so that the angle between plane of D molecule [determined by atoms e, f and g, see Fig. 8(a)] and the axis of SWBNNT increases considerably, even reaches 90° in a SWBNNT with a large diameter, e.g., the (15, 6) SWBNNT [see Fig. 11(b)]. This observation is quite different from the chiral transition in bulk systems. When the D molecule clings to the SWBNNT surface again, its chirality may be changed [see Fig. 11(c)]. We have computed the interaction energies between (15, 6) SWBNNT and D molecule, and find that when chiral transition occurs (at this time, D molecule is almost perpendicular to the nanotube axis), D molecule loses interaction energies [~30 kJ/mol, see Fig. 11(d)], mainly comes from the lost in vdW interactions (the electrostatic interactions between D molecules and nanotube is very small, in the order of 0.1 kJ/mol).

We have also obtained the interaction energy barrier ΔE for the chiral transitions inside different SWBNNTs. The results are displayed in Fig. 10(a) (●, right axis). ΔE is defined as the average interaction energy in the t_2 period, minus the average interaction energy in the t_1 and t_3 periods [see Fig. 11(d)]. It is found that ΔE gradually increases with the diameter of SWBNNTs and the tendency is quite similar to that of the threshold temperature T_C. It appears that the T_C for the D molecule is mainly determined by the transition barrier from a parallel conformation to a perpendicular conformation relative to the nanotube axis. Therefore, we can control the transition temperature by using SWBNNTs with appropriate diameters. To further characterize the effect of confined environments on the chiral transition, we have calculated the free energy of chiral transition for isolated D molecule, and a D molecule inside (13, 4) and (14, 5) SWBNNTs, at the room temperature (300 K). Compared to that of isolated D molecule, the free energy barriers for (13, 4) and (14, 5) SWBNNTs decrease by ~5 kJ/mol and ~3 kJ/mol, respectively (see ref. [24] for more details), indicating that the confined environment can indeed catalyze the enantiomerization of molecules with planar chirality.

In summary, we have performed MD simulations of chiral transition of D molecule (with planar chirality) in SWBNNTs and revealed remarkable effects of nanoscale confinement on molecular chirality. The critical temperature, above which the enantiomerization occurs, increases considerably with the diameter of nanotube, and the frequency of chiral transition decreases exponentially with respect to the reciprocal of temperature. The chiral transitions are found to closely correlate with the orientational transformations of D molecule. Furthermore, the barriers of interaction energies between D molecule and SWBNNT for different orientational states can characterize the chiral transition, implying that the temperature thresholds of chiral transitions can be controlled by nanotubes with appropriate diameters.

These findings provide new insights to the effect of nano-confinement on molecular chirality, and offer some guidance for the safe delivery of the chiral drugs since an unexpected chiral transition may cause serious cytotoxicity.

2.4. Conformational change of small peptides in carbon nanotubes

How proteins fold and unfold in nanoscale confinement has been an open question to the society. Currently, most of the experimental and theoretical studies on protein folding are performed in dilute solutions [71-73]. However, in *vivo*, proteins fold in a heterogeneous, crowded, and confined space, in which the energy landscapes, the folding thermodynamics and kinetics may alter from that in bulk [74-92]. Interestingly in some situations, the confined environment could facilitate the proteins folding to their desired native structures, such as the confinement in chaperonin-assisted folding cavity [93-96], or the exit tunnel of the ribosome [97, 98].

Previous studies using polymer physics models have proposed an entropic stabilization theory, pointing out that the stability of folded protein can be enhanced in confined space because of the reduction of conformational entropy to the unfolded structural ensemble [80, 85, 92, 94]. On the other hand, the additional hydrophobic interaction between the protein and the confined boundary may destabilize the folded state [76-78, 81]. Both the stabilization and destabilization effects due to the confinement were then examined in amino acid side chain level using molecular dynamics simulations by Vaitheeswaran and Thirumalai [99]. In their work, three types of side chain interactions, hydrophobic (Ala:Phe), polar (Ser:Asn) and charged (Lys:Glu), were simulated in a cylinder nanopore confinement with different lengths and diameters, showing that the hydrophobic side chain pair was strongly destabilized and then separated in the confined environment, while both the interactions of polar side chain pair and charged side chain pair were enhanced in the cylindrical confinement [99].

Later, the effect of different confining geometries on protein-folding thermodynamics and kinetics were studied by Mittal and Best [100], in which two proteins, a 3-helix bundle protein prb and protein G, were tested in a coarse-grained model. A quantitative exponential relationship ($R^{-\gamma c}$, where $\gamma c \approx 5/3$) was found between the characteristic size R of the confining boundary and its stabilization effect on the folded state. Surprisingly, the stabilization effect was not relevant to the dimension of the confinement (*e.g.*, planar, cylindrical, or spherical) [100]. The dominant effect of stability and kinetics by confinement was due to the free energy change of the unfolded state in proteins, in which the diffusion coefficients only show difference in the unfolded state basin.

The role of solvent in protein folding kinetics and thermodynamics in confined environment was investigated by Pande's group [81]. In a small representative protein (villin) system, Pande and co-workers found that the protein was promoted to folded state and more unlikely to change to the unfolded state when only the protein was confined [81]. However, the folded state was destabilized when both the protein and waters were confined. Comparing to the bulk, a compact unfolded state was promoted

instead of native state, which points out the confined solvent may be another crucial aspect to the protein folding under nanoscale confinement.

Carbon nanotubes (CNTs) are good cylindrical condiment carriers with hydrophobic surface [9]. CNTs are recognized as promising candidates to be biocompatible cargos for drugs, nucleic acids, and proteins because they can spontaneously penetrate mammalian cells [101, 102]. Towards this goal, lots of efforts have been put on studying the biosafety of using CNTs *in vivo*, where the potential influence of CNTs to the biomolecules need to be carefully investigated [10-19]. Our recent work indicates that four main types of interactions -- hydrophobic interaction, π-π stacking interaction, electrostatic interaction, and cation-π interaction -- could affect the structure and function of protein [103, 104]. However, the interactions of proteins with inner side of CNTs are not fully studied yet. The hydrophobic wall of CNT could drastically change the original strong-polar environment (*e.g.*, water) around proteins. In addition, the CNT confinement could affect the solvent by decreasing its entropy. For example, a 23-residue helical peptide was found unstable in CNT by Ponder's group, in which the change of solvent entropy was considered to be the main reason alter the protein stability [9].

In this section, the stability of protein motifs are systematically investigated in CNT confinement with various secondary structures, including a helix, a beta-sheet, and a hairpin turn. Our simulations show that the stability of tested peptides is mainly dependent on their secondary structural types. Interestingly, the stability of beta-sheet peptides is enhanced by the CNTs confinement, but those stabilized beta-sheets can become totally unfolded when a hairpin turn is added to connect these two beta-sheets. The helical structure was bended inside the CNTs in order to adapt to the curved surface, forming stable coil-coil structures (see Table 3).

System	CNT (15, 15) D = 20 Å[a]	CNT (22, 22) D = 30 Å	Bulk water
Hairpin turn (GB1)	unfolded	unfolded	stable
Single-strand beta Ac-KLVFFAE-NH_2	stable	stable	unstable
Double-strand antiparallel beta Ac-KLVFFAE-NH_2	stabilized	stabilized	unstable
Alpha-helix (26-mer poly-alanine)	coil-coil	coil-coil	stable

a D refers to the diameter of the CNTs

Table 3. Comparison the stability of peptide with various secondary structures in bulk water and under CNTs confinement.

The structure of hairpin turn in CNT confinement was investigated by all-atom MD simulations with explicit solvent. The GB1 hairpin turn (PDB entry 2GB1, residue index 41 to 56) was put into CNTs with diameters of D=20 Å (D20) and 30 Å (D30), respectively [105]. We found both hairpin turns were unfolded to random coils after 30 ns simulations in CNTs of

http://dx.doi.org/10.5772/51453

different sizes [see Figs. 12 and 13(a)]. The hairpin turn was unfolded to a more relaxed form in the larger size CNT, with radius of gyrations (Rg) 10.1 Å in D30 CNT and 6.7 Å in D20 CNT. Both unfolding processes were started at the turn segment, where the hydrogen bonds formed in the beta region were broken gradually (Fig. 13b). Meanwhile, the aromatic side-chains of Trp_{43}, Tyr_{45}, and Phe_{52} in the beta-region were tightly stuck to the inner wall of CNT by their strong π-π stacking interactions. A helix-like structure was formed in the turn segment [Figs. 12(b) and (d)]. The φ/ψ backbone dihedral angle distributions indicated the alpha-helix and poly-Pro II were the dominant conformations in the CNT confinements for hairpin turns [Figs.13 (c) and (d)].

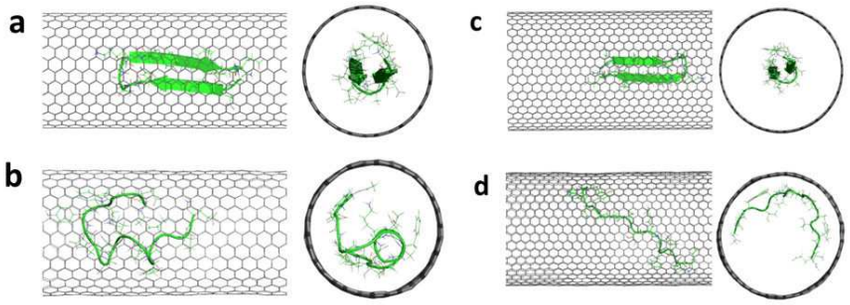

Figure 12. Conformational changes of hairpin turn GB1 inside CNTs. (**a**) and (**b**) The starting structures and the final snapshots of hairpin turn in CNTs with D = 20 Å. (**c**) and (**d**) The starting structures and the final snapshots of hairpin turn in CNTs with D = 30 Å. The final snapshots were obtained from 100 ns MD simulations.

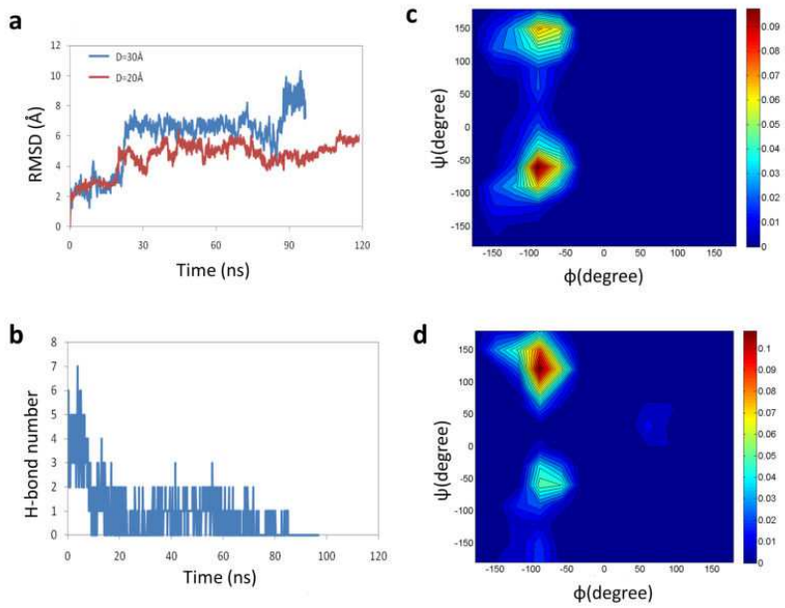

Figure 13. Conformational change of hairpin backbone. (**a**) The RMSD values of hairpin backbone by comparing each snapshot to the starting native structure during the simulations. (**b**) The number of hydrogen bonds formed in the zip

region between backbone atoms. (**c**) and (**d**) Distribution of backbone dihedral angles (φ and ψ) of hairpin turn in D20 and D30 CNTs.

The polyalanine chain was then utilized as the model system to study the stability of helix in CNT confinement. A 26-residue alanine chain was started from alpha-helix form. At the beginning of the simulations, the alanine chain was put in the middle of the CNT along the tube direction [Figs. 14(a) and (c)]. To our surprise, in just a few nanosceonds of the simulations, the entire alanine chain was quickly stuck to the inner side of CNT wall for all sizes of CNTs. Then the helix was bent to adapt the curved surface of CNT and extended along the unit vector, and finally the alpha-hliex turned to the coil-coil superhelix structure [Figs. 14(b) and (d)]. We performed 3 extra independent simulations for each size of CNT systems to conform the fast conformational changes and the final coil-coil superhelix structure for all the alanine chains. The superhelix conformation is an important feature to design proteins that can wrap CNTs, which has been successfully applied to virus-like protein assemblies on CNT surfaces in DeGrado's group [106]. Our simulations indicate that similar strategy could be applied to wrap inner side of CNTs with preferred of coil-coil superhelix structure.

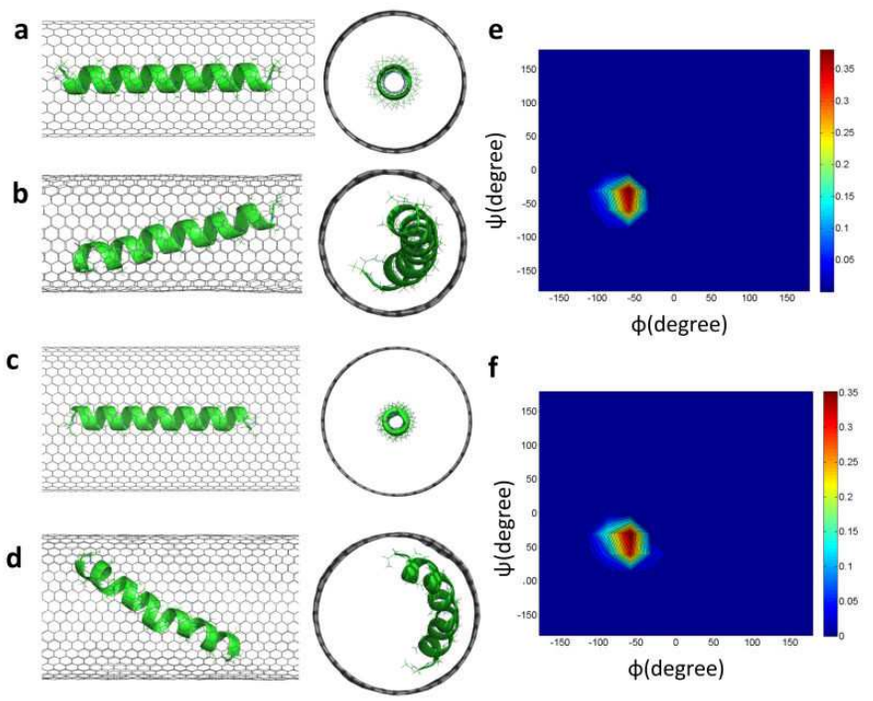

Figure 14. Conformational changes of helical polyalanine inside CNTs. (**a**) and (**b**) The starting structures and the final snapshots of polyalanine in CNTs with D=20 Å. (**c**) and (**d**) The starting structures and the final snapshots of polyalanine in CNTs with D=30 Å. The final snapshots were obtained from 100 ns MD simulations. (**e**) and (**f**) Distribution of backbone dihedral angles (φ and ψ) in polyalanine in D20 and D30 CNTs.

For beta-strand structure, we used Alzheimer amyloid-$\beta_{16\text{-}22}$ peptides (Ace-KLVFFAE-NH_2) as an example. Both single- and double-strand beta were put into the center of CNT (15, 15) [Figs. 15(a) and (c)]. The anti-parallel double-strand sheet was stable inside the CNT during the simulation; in each strand, two phenylalanine were stuck to the inside wall of CNT, and

http://dx.doi.org/10.5772/51453

the backbone-backbone hydrogen bonds between two strands were well kept [Figs. 15(d) and (f)]. For single beta strand, large fluctuations can be seen at two charged terminals. However, the middle 4-residue (with sequence "LVFFA") still remained the beta shape [Figs. 15(b) and (e)], which was much more stable than single strand in bulk water. Our recently theoretical investigation has shown that the hydrophobic effect plays a significant role in protein self-assembly in water, in which the "dewetting transition" can be induced by the hydrophobic interaction between two strands in both amyloid-β peptides (KLVFFAE) and $hIAPP_{22-27}$ peptides (NFGAIL) [107, 108]. Our simulations confirm that beta-strand conformation can be stabilized in hydrophobic environment, which could further promote the formation of protofilaments and form amyloid fibrils. Further study is needed to confirm the role of hydrophobic confinement in facilitating the formation of amyloid fibrils.

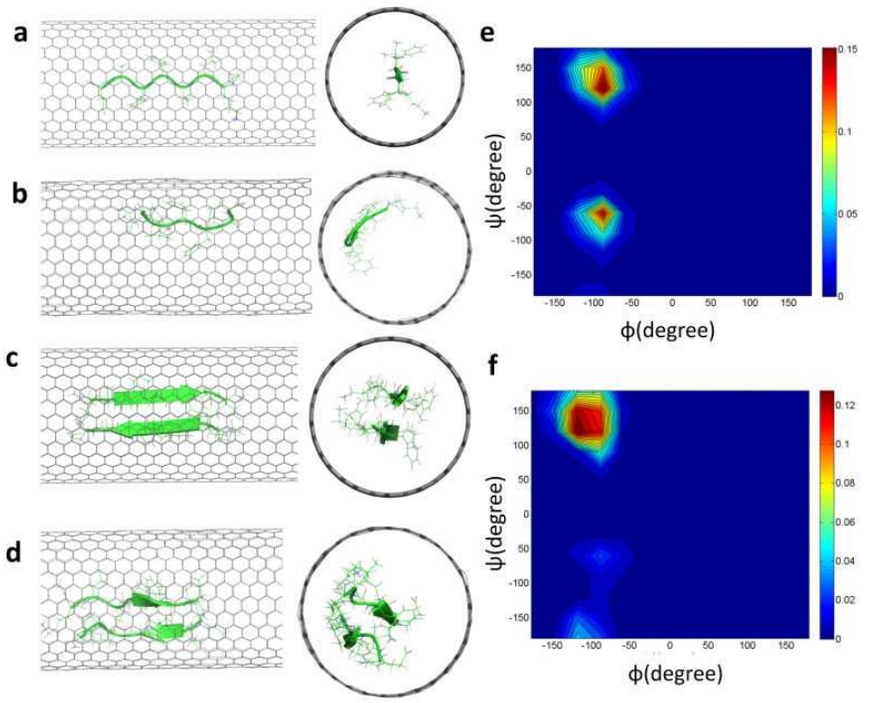

Figure 15. Conformational changes of beta-sheet(s) inside CNTs. (**a**) and (**b**) The starting structures and the final snapshots of single-strand amyloid-beta in CNTs with D=20 Å. (**c**) and (**d**) The starting structures and the final snapshots of double-strand antiparallel Amyloid-beta sheets in CNTs with D=20 Å. The final snapshots were obtained from 100 ns MD simulations. (**e**) and (**f**) Distribution of backbone dihedral angles (φ and ψ) in single-strand and double-strand amyloid-beta sheet(s).

In conclusion, we have investigated three important secondary structural motifs in protein – hairpin turn, helix, and beta-sheet – with CNT confinements by all-atom MD simulations. We find only beta-strand conformation is stabilized in the CNTs. The alpha-helical polyalanine is turned to form coil-coil superhelix structure in order to adapt the curved surface of CNTs. The hairpin turn becomes the most unstable structure in the CNT which totally unfolds to random coil structure and sticks to the CNT walls. Therefore, it is hard to make simple conclusions that CNT confinement could stabilize or destabilize the protein structures.

The conformation of protein in the CNT confinement could be largely dependent on its residue types and building motifs.

3. Conclusion

In this book chapter, we review some of our recent computational works, including: i) the water-mediated signal conversion and multiplication with Y-SWNT; ii) structure, dynamics, and transportation of urea wire and the phenomenon of urea-induced drying inside SWNT; iii) remarkable effect of nanoscale confinement on molecular chirality; and iv) conformational changes of various peptides under nanoscale confinement. These studies provide a deeper understanding towards the unique structure and behaviors of small molecules (water and small organic molecules) and peptides under nanoscale confinement, and demonstrate potential wide implications in nanoscale signal processing, single-file transportation, drug delivery, and even cytotoxicity.

Acknowledgements

We thank Prof. Zhigang Wang, and Dr. Yusong Tu for helpful discussions. This research is supported in part by grants from Zhejiang Provincial Natural Science Foundation of China (Grant No. LY12A04007), the China Postdoctoral Science Foundation (Grant No. 201104738), and the Fundamental Research Funds for the Central Universities. RZ acknowledges the support from the IBM BlueGene Science Program.

Author details

Peng Xiu[3], Zhen Xia[1,2] and Ruhong Zhou[1,4]

1 Computational Biology Center, IBM Thomas J. Watson Research Center, Yorktown Heights, NY 10598

2 Department of Biomedical Engineering, The University of Texas at Austin, Austin , TX 78712

3 Department of Engineering Mechanics, and Soft Matter Research Center, Zhejiang University, Hangzhou , 310027, China

4 Department of Chemistry, Columbia University , New York, NY 10027

References

[1] Hummer, G., Rasaiah, J. C., & Noworyta, J. P. (2001). Water conduction through the hydrophobic channel of a carbon nanotube. *Nature* [414], 188-190.

[2] Koga, K., Gao, G. T., Tanaka, H., et al. (2001). Formation of ordered ice nanotubes inside carbon nanotubes. *Nature* [412], 802-805.

[3] Ball, P. (2008). Water as an active constituent in cell biology. *Chem. Rev.* [108], 74-108.

[4] Holt, J. K., Park, H. G., Wang, Y. M., et al. (2006). Fast mass transport through sub-2-nanometer carbon nanotubes. *Science* [312], 1034-1037.

[5] Chen, S. M., Wu, G. Z., Sha, M. L., et al. (2007). Transition of ionic liquid [bmim][PF6] from liquid to high-melting-point crystal when confined in multiwalled carbon nanotubes. *J. Am. Chem. Soc.* [129], 2416.

[6] Su, Z., Zhu, S., Donkor, A. D., et al. (2011). Controllable Delivery of Small-Molecule Compounds to Targeted Cells Utilizing Carbon Nanotubes. *J. Am. Chem. Soc.* [133], 6874-6877.

[7] Tasis, D., Tagmatarchis, N., Bianco, A., et al. (2006). Chemistry of carbon nanotubes. *Chem. Rev.* [106], 1105-1136.

[8] Pan, X. L., Fan, Z. L., Chen, W., et al. (2007). Enhanced ethanol production inside carbon-nanotube reactors containing catalytic particles. *Nat. Mater.* [6], 507-511.

[9] Sorin, E. J., & Pande, V. S. (2006). Nanotube confinement denatures protein helices. *J. Am. Chem. Soc.* [128], 6316-6317.

[10] Zanello, L. P., Zhao, B., Hu, H., et al. (2006). Bone cell proliferation on carbon nanotubes. *Nano Lett.* [6], 562-567.

[11] Prato, M., Kostarelos, K., & Bianco, A. (2008). Functionalized carbon nanotubes in drug design and discovery. *Acc. Chem. Res.* [41], 60-68.

[12] Bhirde, A. A., Patel, V., Gavard, J., et al. (2009). Targeted Killing of Cancer Cells in Vivo and in Vitro with EGF-Directed Carbon Nanotube-Based Drug Delivery. *ACS Nano* [3], 307-316.

[13] Thakare, V. S., Das, M., Jain, A. K., et al. (2010). Carbon nanotubes in cancer theragnosis. *Nanomedicine* [5], 1277-1301.

[14] Bi, S. P., Zhang, J., & Cheng, J. J. (2009). Call from China for joint nanotech toxicity-testing effort. *Nature* [461], 593.

[15] Donaldson, K., & Poland, C. A. (2009). NANOTOXICOLOGY New insights into nanotubes. *Nat. Nanotechnol.* [4], 708-710.

[16] Gilbert, N. (2009). Nanoparticle safety in doubt. *Nature* [460], 937.

[17] Nel, A., Xia, T., Madler, L., et al. (2006). Toxic potential of materials at the nanolevel. *Science*, 2006(311), 622-627.

[18] Service, R. F. (2000). Is nanotechnology dangerous? *Science*, 2000(290), 1526-1527.

[19] Zhao, Y. L., Xing, G. M., & Chai, Z.F. (2008). Nanotoxicology: Are carbon nanotubes safe? *Nat. Nanotechnol.* , 2008(3), 191-192.

[20] Ge, C. C., Du, J. F., Zhao, L. N., et al. (2011). Binding of blood proteins to carbon nanotubes reduces cytotoxicity. *Proc. Natl. Acad. Sci. U. S. A.* , 2011(108), 16968-16973.

[21] Tu, Y. S., Xiu, P., Wan, R. Z., et al. (2009). Water-mediated signal multiplication with Y-shaped carbon nanotubes. *Proc. Natl. Acad. Sci. U. S. A.* , 2009(106), 18120-18124.

[22] Xiu, P., Yang, Z. X., Zhou, B., & et, al. . (2011). Urea-Induced Drying of Hydrophobic Nanotubes: Comparison of Different Urea Models. *J. Phys. Chem. B* , 2011(115), 2988-2994.

[23] Xiu, P., Tu, Y., Tian, X., et al. (2012). Molecular wire of urea in carbon nanotube: a molecular dynamics study. *Nanoscale*, 2012(4), 652-658.

[24] Zhang, R. Q., Wang, Z. G., Wang, C. L., et al. (2010). Size Dependence of Nanoscale Confinement on Chiral Transformation. *Chem. Eur. J.* , 2010(16), 6482-6487.

[25] Tu, Y. S., Zhou, R. H., & Fang, H. P. (2010). Signal transmission, conversion and multiplication by polar molecules confined in nanochannels. *Nanoscale*, 2010(2), 1976-1983.

[26] Kwok, K., & Ellenbogen, J. (2002). Moletronics: future electronics. *Materials Today* , 2002(5), 28-37.

[27] Xu, H. Q. (2005). Nanotubes: The logical choice for electronics? *Nat. Mater.*, 2005(4), 649-650.

[28] Koenig, D. R., Weig, E. M., & Kotthaus, J. P. (2008). Ultrasonically driven nanomechanical single-electron shuttle. *Nat Nano*, 2008(3), 482-485.

[29] Litvinchuk, S., Tanaka, H., Miyatake, T., et al. (2007). Synthetic pores with reactive signal amplifiers as artificial tongues. *Nat. Mater.* [6], 576-580.

[30] Köfinger, J., Hummer, G., & Dellago, C. (2008). Macroscopically ordered water in nanopores. *Proc. Natl. Acad. Sci. U. S. A.* [105], 13218-13222.

[31] Li, J. Y., Gong, X. J., Lu, H. J., et al. (2007). Electrostatic gating of a nanometer water channel. *Proc. Natl. Acad. Sci. U. S. A.* [104], 3687-3692.

[32] Papadopoulos, C., Rakitin, A., Li, J., et al. (2000). Electronic Transport in Y-Junction Carbon Nanotubes. *Phys. Rev. Lett.* , 85, 3476 -3479 .

[33] Terrones, M., Banhart, F., Grobert, N., et al. (2002). Molecular Junctions by Joining Single-Walled Carbon Nanotubes. *Phys. Rev. Lett.* , 89, 075505 .

[34] Gothard, N., Daraio, C., Gaillard, J., et al. (2004). Controlled Growth of Y-Junction Nanotubes Using Ti-Doped Vapor Catalyst. *Nano Lett.* [4], 213-217.

[35] Bandaru, P. R., Daraio, C., Jin, S., et al. (2005). Novel electrical switching behaviour and logic in carbon nanotube Y-junctions. *Nat. Mater.* [4], 663-666.

[36] Lindahl, E., Hess, B., & van der Spoel, D. (2001). GROMACS 3.0: a package for molecular simulation and trajectory analysis. *J. Mol. Modeling* [7], 306-317.

[37] Jorgensen, W. L., Chandrasekhar, J., Madura, J. D., et al. (1983). Comparison of Simple Potential Functions for Simulating Liquid Water. *J. Chem. Phys.* [79], 926-935.

[38] Luna, V. M., Chen, Y., Fee, J. A., et al. (2008). Crystallographic Studies of Xe and Kr Binding within the Large Internal Cavity of Cytochrome ba3 from Thermus thermophilus: Structural Analysis and Role of Oxygen Transport Channels in the Heme-Cu Oxidases. *Biochemistry* , 47(47), 4657-4665.

[39] Moustafa, I. M., Foster, S., Lyubimov, A. Y., et al. (2006). Crystal Structure of LAAO from Calloselasma rhodostoma with an l-Phenylalanine Substrate: Insights into Structure and Mechanism. *J. Mol. Biol.* , 2006(364), 991-1002.

[40] Berezhkovskii, A., & Hummer, G. (2002). Single-file transport of water molecules through a carbon nanotube. *Phys. Rev. Lett.* , 89, 064503 .

[41] Best, R. B., & Hummer, G. (2005). Reaction coordinates and rates from transition paths. *Proc. Natl. Acad. Sci. U. S. A.* , 2005(102), 6732-6737.

[42] Kofinger, J., Hummer, G., & Dellago, C. (2008). Macroscopically ordered water in nanopores. *Proc. Natl. Acad. Sci. U. S. A.* , 2008(105), 13218-13222.

[43] de Groot, B. L., & Grubmuller, H. (2001). Water permeation across biological membranes: Mechanism and dynamics of aquaporin-1 and GlpF. *Science* [294], 2353-2357.

[44] Tajkhorshid, E., Nollert, P., Jensen, M. O., et al. (2002). Control of the selectivity of the aquaporin water channel family by global orientational tuning. *Science* [296], 525-530.

[45] Raghavender, U. S., Kantharaju, , Aravinda, S., et al. (2010). Hydrophobic Peptide Channels and Encapsulated Water Wires. *J. Am. Chem. Soc.* [132], 1075-1086.

[46] Wan, R. Z., Li, J. Y., Lu, H. J., et al. (2005). Controllable water channel gating of nanometer dimensions. *J. Am. Chem. Soc.* [127], 7166-7170.

[47] Li, J. Y., Gong, X. J., Lu, H. J., et al. (2007). Electrostatic gating of a nanometer water channel. *Proc. Natl. Acad. Sci. U. S. A.* [104], 3687-3692.

[48] Wan, R. Z., Lu, H. J., Li, J. Y., et al. (2009). Concerted orientation induced unidirectional water transport through nanochannels. *Phys. Chem. Chem. Phys.* [11], 9898-9902.

[49] Reddy, G., Straub, J. E., & Thirumalai, D. (2010). Dry amyloid fibril assembly in a yeast prion peptide is mediated by long-lived structures containing water wires. *Proc. Natl. Acad. Sci. U. S. A.* [107], 21459-21464.

[50] Cao, Z., Peng, Y. X., Yan, T. Y., et al. (2010). Mechanism of Fast Proton Transport along One-Dimensional Water Chains Confined in Carbon Nanotubes. *J. Am. Chem. Soc.* [132], 11395-11397.

[51] Jensen, M. O., Borhani, D. W., Lindorff-Larsen, K., et al. (2010). Principles of conduction and hydrophobic gating in K+ channels. *Proc. Natl. Acad. Sci. U. S. A.* [107], 5833-5838.

[52] Dong, K., Zhou, G. H., Liu, X. M., et al. (2009). Structural Evidence for the Ordered Crystallites of Ionic Liquid in Confined Carbon Nanotubes. *J. Phys. Chem. C* [113], 10013-10020.

[53] Chaban, V. (2010). Filling carbon nanotubes with liquid acetonitrile. *Chem. Phys. Lett.* [496], 50-55.

[54] Liu, Y., Consta, S., & Goddard, W. A. (2010). Nanoimmiscibility: Selective Absorption of Liquid Methanol-Water Mixtures in Carbon Nanotubes. *J. Nanosci. Nanotechnol.* , 2010(10), 3834-3843.

[55] Lee, J., & Aluru, N. R. (2010). Separation of gases from gas-water mixtures using carbon nanotubes. *Appl. Phys. Lett.* , 96, 133108 .

[56] Kalra, A., Hummer, G., & Garde, S. (2004). Methane partitioning and transport in hydrated carbon nanotubes. *J. Phys. Chem. B* [108], 544-549.

[57] Knepper, M. A., & Mindell, J. A. (2009). STRUCTURAL BIOLOGY Molecular coin slots for urea. *Nature* [462], 733-734.

[58] Levin, E. J., Quick, M., & Zhou, M. (2009). Crystal structure of a bacterial homologue of the kidney urea transporter. *Nature*, 2009(462), 757-761.

[59] Weerasinghe, S., & Smith, P. E. (2003). A Kirkwood-Buff derived force field for mixtures of urea and water. *J. Phys. Chem. B* [107], 3891-3898.

[60] Duffy, E. M., Severance, D. L., & Jorgensen, W. L. (1993). UREA- POTENTIAL FUNCTIONS, LOG-P, AND FREE-ENERGY OF HYDRATION. *Isr. J. Chem.* , 1993(33), 323-330.

[61] Smith, L. J., Berendsen, H. J. C., & van Gunsteren, W. F. (2004). Computer simulation of urea-water mixtures: A test of force field parameters for use in biomolecular simulation. *J. Phys. Chem. B* [108], 1065-1071.

[62] Hess, B., Kutzner, C., van der Spoel, D., et al. (2008). GROMACS 4: Algorithms for highly efficient, load-balanced, and scalable molecular simulation. *J. Chem. Theory Comput.* , 2008(4), 435-447.

[63] Mac, Kerell. A. D., Bashford, D., Bellott, M., et al. (1998). All-atom empirical potential for molecular modeling and dynamics studies of proteins. *J. Phys. Chem. B* [102], 3586-3616.

[64] Sorin, E. J., & Pande, V. S. (2005). Exploring the helix-coil transition via all-atom equilibrium ensemble simulations. *Biophys. J.* [88], 2472-2493.

[65] Hua, L., Zhou, R. H., Thirumalai, D., et al. (2008). Urea denaturation by stronger dispersion interactions with proteins than water implies a 2-stage unfolding. *Proc. Natl. Acad. Sci. U. S. A.* [105], 16928-16933.

[66] Agranat, I., Caner, H., & Caldwell, A. (2002). Putting chirality to work: The strategy of chiral switches. *Nat. Rev. Drug Discovery* [1], 753-768.

[67] Eriksson, T., Björkman, S., Roth, B., et al. (1998). Enantiomers of thalidomide: blood distribution and the influence of serum albumin on chiral inversion and hydrolysis. *Chirality* [10], 223-228.

[68] Blaschke, G., Kraft, H., , P., & Markgraf, H. (1980). Chromatographische Racemattrennungen, X. Racemattrennung des Thalidomids und anderer Glutarimid-Derivate. *Chem. Ber.* [113], 2318-2322.

[69] Hembury, G. A., Borovkov, V. V., & Inoue, Y. (2008). Chirality-sensing supramolecular systems. *Chem. Rev.* [108], 1-73.

[70] Umeda, H., Takagi, M., Yamada, S., et al. (2002). Quantum control of molecular chirality: Optical isomerization of difluorobenzo c phenanthrene. *J. Am. Chem. Soc.* [124], 9265-9271.

[71] Fersht, A. R., Matouschek, A., & Serrano, L. (1992). The folding of an enzyme.1. Theory of protein engineering analysis of stability and pathway of protein folding. *J. Mol. Biol.* [224], 771-782.

[72] Snow, C. D., Sorin, E. J., Rhee, Y. M., et al. (2005). How well can simulation predict protein folding kinetics and thermodynamics? *Annu. Rev. Biophys. Biomol. Struct.*, 43-69.

[73] Zhou, R., Huang, X., Margulis, C. J., et al. (2004). Hydrophobic collapse in multidomain protein folding. *Science* [305], 1605-9.

[74] Betancourt, M. R., & Thirumalai, D. (1999). Exploring the kinetic requirements for enhancement of protein folding rates in the GroEL cavity. *J. Mol. Biol.* [287], 627-644.

[75] Bolis, D., Politou, A. S., Kelly, G., et al. (2004). Protein stability in nanocages: A novel approach for influencing protein stability by molecular confinement. *J. Mol. Biol.* [336], 203-212.

[76] Cheung, M. S., & Thirumalai, D. (2006). Nanopore-protein interactions dramatically alter stability and yield of the native state in restricted spaces. *J. Mol. Biol.* [357], 632-643.

[77] Eggers, D. K., & Valentine, J. S. (2001). Crowding and hydration effects on protein conformation: A study with sol-gel encapsulated proteins. *J. Mol. Biol.* [314], 911-922.

[78] Eggers, D. K., & Valentine, J. S. (2001). Molecular confinement influences protein structure and enhances thermal protein stability. *Protein Sci.* [10], 250-261.

[79] Ellis, R. J., & Minton, A. P. (2003). Cell biology-. *Join the crowd. Nature* [425], 27-28.

[80] Klimov, D. K., Newfield, D., & Thirumalai, D. (2002). Simulations of beta-hairpin folding confined to spherical pores using distributed computing. *Proc. Natl. Acad. Sci. U. S. A.* [99], 8019-8024.

[81] Lucent, D., Vishal, V., & Pande, V. S. (2007). Protein folding under confinement: A role for solvent. *Proc. Natl. Acad. Sci. U. S. A.* [104], 10430-10434.

[82] Minton, A. P. (2000). Implications of macromolecular crowding for protein assembly. *Curr. Opin. Struct. Biol.* [10], 34-39.

[83] Ravindra, R., Shuang, Z., Gies, H., et al. (2004). Protein encapsulation in mesoporous silicate: The effects of confinement on protein stability, hydration, and volumetric properties. *J. Am. Chem. Soc.* [126], 12224-12225.

[84] Zhou, H.X. (2007). Helix formation inside a nanotube: Possible influence of backbone-water hydrogen bonding by the confining surface through modulation of water activity. *J. Chem. Phys.*, 127, 245101.

[85] Zhou, H. X., & Dill, K. A. (2001). Stabilization of proteins in confined spaces. *Biochemistry* [40], 11289-11293.

[86] Ellis, R. J. (2001). Macromolecular crowding: obvious but underappreciated. *Trends Biochem. Sci.* [26], 597-604.

[87] Friedel, M., Sheeler, D. J., & Shea, J. E. (2003). Effects of confinement and crowding on the thermodynamics and kinetics of folding of a minimalist beta-barrel protein. *J. Chem. Phys.* [118], 8106-8113.

[88] Stagg, L., Zhang, S., , Q., Cheung, M. S., et al. (2007). Molecular crowding enhances native structure and stability of alpha/beta protein flavodoxin. *Proc. Natl. Acad. Sci. U. S. A.* [104], 18976-18981.

[89] van den, Berg. B., Ellis, R. J., & Dobson, C. M. (1999). Effects of macromolecular crowding on protein folding and aggregation. *EMBO J.* [18], 6927-6933.

[90] Zhou, H., & , X. (2008). Protein folding in confined and crowded environments. *Arch. Biochem. Biophys.* [469], 76-82.

[91] Zhou, H., , X., Rivas, G., & Minton, A. P. (2008). Macromolecular crowding and confinement: Biochemical, biophysical, and potential physiological consequences. *In Annual Review of Biophysics*, 375-397.

[92] Thirumalai, D., Klimov, D. K., & Lorimer, G. H. (2003). Caging helps proteins fold. *Proc. Natl. Acad. Sci. U. S. A.* [100], 11195-11197.

[93] Thirumalai, D., & Lorimer, G. H. (2001). Chaperonin-mediated protein folding. *Annu. Rev. Biophys. Biomol. Struct.* [30], 245-269.

[94] Takagi, F., Koga, N., & Takada, S. (2003). How protein thermodynamics and folding mechanisms are altered by the chaperonin cage: Molecular simulations. *Proc. Natl. Acad. Sci. U. S. A.* [100], 11367-11372.

[95] Jewett, A. I., Baumketner, A., & Shea, J. E. (2004). Accelerated folding in the weak hydrophobic environment of a chaperonin cavity: Creation of an alternate fast folding pathway. *Proc. Natl. Acad. Sci. U. S. A.* [101], 13192-13197.

[96] Baumketner, A., Jewett, A., & Shea, J. E. (2003). Effects of confinement in chaperonin assisted protein folding: Rate enhancement by decreasing the roughness of the folding energy landscape. *J. Mol. Biol.* [332], 701-713.

[97] Woolhead, C. A., Mc Cormick, P. J., & Johnson, A. E. (2004). Nascent membrane and secretory proteins differ in FRET-detected folding far inside the ribosome and in their exposure to ribosomal proteins. *Cell*, 2004(116), 725-736.

[98] Ziv, G., Haran, G., & Thirumalai, D. (2005). Ribosome exit tunnel can entropically stabilize alpha-helices. *Proc. Natl. Acad. Sci. U. S. A.* [102], 18956-18961.

[99] Vaitheeswaran, S., & Thirumalai, D. (2008). Interactions between amino acid side chains in cylindrical hydrophobic nanopores with applications to peptide stability. *Proc. Natl. Acad. Sci. U. S. A.* [105], 17636-17641.

[100] Mittal, J., & Best, R. B. (2008). Thermodynamics and kinetics of protein folding under confinement. *Proc. Natl. Acad. Sci. U. S. A.* [105], 20233-20238.

[101] Kam, N. W. S., Liu, Z., & Dai, H. J. (2005). Functionalization of carbon nanotubes via cleavable disulfide bonds for efficient intracellular delivery of siRNA and potent gene silencing. *J. Am. Chem. Soc.* [127], 12492-12493.

[102] Kam, N. W. S., Liu, Z. A., & Dai, H. J. (2006). Carbon nanotubes as intracellular transporters for proteins and DNA: An investigation of the uptake mechanism and pathway. *Angew. Chem. Int. Ed.* [45], 577-581.

[103] Zuo, G. H., Huang, Q., Wei, G. H., et al. (2010). Plugging into Proteins: Poisoning Protein Function by a Hydrophobic Nanoparticle. *ACS Nano* [4], 7508-7514.

[104] Yang, Z., Wang, Z., Tian, X., et al. (2012). Amino acid analogues bind to carbon nanotube via pi-pi interactions: Comparison of molecular mechanical and quantum mechanical calculations. *J. Chem. Phys*, 136, 025103.

[105] Gronenborn, A. M., Filpula, D. R., Essig, N. Z., & et, al. . (1991). A Novel, Highly Stable Fold of the Immunoglobulin Binding Domain of Streptococcal Protein-G. *Science* [253], 657-661.

[106] Grigoryan, G., Kim, Y. H., Acharya, R., et al. (2011). Computational Design of Virus-Like Protein Assemblies on Carbon Nanotube Surfaces. *Science*, 2011(332), 1071-1076.

[107] Krone, M. G., Hua, L., Soto, P., et al. (2008). Role of water in mediating the assembly of Alzheimer amyloid-beta a beta 16-22 protofilaments. *J. Am. Chem. Soc.* [130], 11066-11072.

[108] Yang, Z. X., Shi, B. Y., Lu, H. J., et al. (2011). Dewetting Transitions in the Self-Assembly of Two Amyloidogenic beta-Sheets and the Importance of Matching Surfaces. *J. Phys. Chem. B* [115], 11137-11144.